JPSE (Journal of Physical Science and Engineering), Vol. 9, No. 2, 2024, Page 49–65
DOI: 10.17977/um024v9i22024p49-65

JPSE
(Journal of Physical Science and Engineering)

http://journal2.um.ac.id/index.php/jpse
EISSN: 2541-2485

The Influences of Carbon Composition on the Performance of Zn-$Mn_{0.25}Fe_{2.75}O_4$@C Thin Films as Zinc-Ion Battery Electrodes

Received
26 May 2024

Revised
26 June 2024

Accepted
27 July 2024

Available online
31 October 2024

Mohammad Naim Bahar[1], Eny Latifah[1], Nadiya Miftachul Chusna[1], Kormil Saputra[3,4], Fadhil Fathurochman[1], Abdul Majeed Himat[5], and Sunaryono Sunaryono[1,2*]

[1] Department of Physics, Faculty of Mathematics and Natural Sciences, Universitas Negeri Malang, Jl. Semarang No. 5, Malang 65145, Indonesia
[2] Centre of Advanced Materials for Renewable Energy, Universitas Negeri Malang, Jalan Semarang No. 5, Malang 65145, Indonesia
[3] Department of Physics, Faculty of Mathematics and Natural Sciences, Universitas Brawijaya, Jl. Veteran No.10-11, Malang, East Java 65145, Indonesia
[4] Physics Study Program, Universitas Mataram, Jl. Majapahit No.62, Gomong, Kec. Selaparang, Mataram, Nusa Tenggara Barat. 83115, Indonesia
[5] Physics of Magnetism and Photonics Research Division, Physics Program Study, Faculty of Mathematics and Natural Sciences, Jl. Ganesha 10, Bandung, West Java, 40132, Indonesia

*Corresponding Author's E-mail: sunaryono.fmipa@um.ac.id

Abstract

Batteries based on Zinc-ion (ZIB) have a high capacity, low cost, low redox potential, and impressive electrochemical stability in water due to their hydrogen evolution. Fe_3O_4 NPs with carbon coated can significantly increase the electrical conductivity of battery. This study investigates the impact of carbon addition on the performance of Zn-$Mn_{0.25}Fe_{2.75}O_4$@C as an electrode material for zinc-ion batteries. The research focuses on developing Zn-$Mn_{0.25}Fe_{2.75}O_4$@C, which combines the advantages of zinc-ion batteries with the improved magnetic and electrical properties of magnetite materials. The material was synthesized using a spin coating method and characterized by X-ray diffraction (XRD), Fourier transform infrared spectroscopy (FTIR), vibrating sample magnetometry (VSM), transmission electron microscopy (TEM), cyclic voltammetry (CV), and charge-discharge (CD) tests. The addition of carbon was found to enhance specific capacitance, energy density, power density, cycle stability, and magnetic properties of the battery electrodes. FTIR characterization indicated the presence of O-H, C-O, Fe-O, Mn-O, C=C, C-N, and C=O groups. XRD revealed a cubic crystal structure with particle sizes between 6.10 nm and 11.53 nm. VSM analysis demonstrated a reduction in magnetization, coercivity, and magnetic remanence with carbon addition. TEM analysis showed an average particle size of 11.5 nm and aggregation of magnetite nanoparticles. CV results indicated the significant potential for Zn-$Mn_{0.25}Fe_{2.75}O_4$@C as a battery electrode with the highest specific capacitance in MCF2. Charge-discharge tests highlighted that MCF2 is ideal for large energy storage, MCF3 for fast charging, and MCF4 for low-performance applications.

Keywords: zinc-ion battery, $Mn_{0.25}Fe_{2.75}O_4$@C nanocomposites, Zn-$Mn_{0.25}Fe_{2.75}O_4$@C thin films, battery electrode.

1. Introduction

The battery is one of the electric cells used to store chemical energy for conversion into electrical energy [1]. There are numerous types of batteries that we encounter in our daily lives. One of these types is single-use batteries, and another is rechargeable batteries, which have their respective advantages and disadvantages. Batteries typically contain various chemical substances, including mercury, manganese, lead, nickel, lithium, and cadmium, which are commonly found in secondary batteries [2]. Thus, despite technological advancements, the performance of batteries remains unsatisfactory for evolving globalization. Among the technologies mentioned above, the lithium-ion battery (LIB) is considered a significant milestone in energy storage. The future of LIB in large-scale applications is hindered by several important factors, such as cost, lifespan, and safety issues [3],[4].

Additionally, other types of batteries, known as aqueous batteries, use water-based electrolytes, which have natural advantages in the factors above compared to expensive and flammable non-aqueous LIBs. Another benefit of aqueous batteries is lower fabrication costs, as they do not require strictly controlled oxygen and water production environments. Advances in aqueous battery systems have been rapid in recent years, including monovalent systems with Li^+, Na^+, and K^+ cations as well as divalent systems with Mg^{2+} and Zn^{2+} [5], [6]. Due to their low cost and high operational safety, water-rechargeable batteries are considered a promising class of batteries for grid-scale electrochemical energy storage. Moreover, compared to non-aqueous electrolytes, aqueous electrolytes offer much higher ionic conductivity, supporting high-rate capabilities.

Recently, rechargeable multivalent ion batteries such as zinc-ion batteries (ZIBs), aluminum-ion batteries (AIBs), and magnesium-ion batteries (MIBs) have attracted many researchers due to their high volumetric energy density (based on metal anodes, Zn: 5851 mA h mL^{-1}, Al: 8046 mA h mL^{-1}, Mg: 3833 mA h mL^{-1}) [7], [8],[9],[10]. Aqueous zinc-ion batteries (ZIBs) based on chemical Zn^{2+} intercalation have received considerable attention among researchers due to their high capacity (820 mA h/g), abundance, low cost, low redox potential (-0.76 V vs. standard hydrogen electrode), and impressive electrochemical stability in water due to their high hydrogen evolution overpotential [11].

Furthermore, dendritic zinc issues in alkaline zinc cells can be addressed by replacing the alkaline electrolyte with a mildly acidic (or slightly acidic) neutral solution, which in turn reduces environmental impact and operational costs [12]. In their development, magnetite materials have been combined with various support materials to enhance mechanical properties and energy capacity. Among them, Zhang et al. synthesized Fe_3O_4/FeS_2 as a high-performance electrocatalyst for oxygen evolution reactions and a zinc-air battery, resulting in a specific energy capacity of about 560 mAh.gzn^{-1} and significant cycle stability [13]. Meanwhile, Han synthesized Fe_3O_4@CNF from cellulose acetate in Li-Ion batteries, producing a specific energy capacity of 773.6 mAh and 596.5 mAh g^{-1} after 300 cycles [14]. Additionally, Wang et al. developed a double-buffering strategy to boost the lithium storage potential of Fe_3O_4 with MIL-100 (Fe) MOF framework embedded on graphene oxide, as a template arranged through an in-situ solvothermal approach, transforming into well-dispersed ultrafine carbon-coated Fe_3O_4-QDs, embedded with well-dispersed, and mesoporous (4 nm) embedded on reduced graphene oxide (Fe_3O_4-QDs@C/rGO), by pyrolysis. This strategy resulted in high reversible capacity with prolonged cyclic stability after 2000 cycles (505 mAh g^{-1} at 2.0 A g^{-1}) [15]. In some of these studies, the Fe_3O_4/FeS_2 nanocomposite material has lower specific energy compared to the carbon-based Fe_3O_4@CNF nanocomposite. This weakness presents an opportunity to combine carbon-based materials with magnetite materials. Moreover, in nanocomposite materials like Fe_3O_4-QDs@C/rGO, the addition of carbon material enhances cyclic stability, as evident from cycles up to 2000 repetitions. Another drawback is the lower magnetization side of Fe_3O_4, thus doping with Mn ions will enhance the magnetization ability, which in turn increases prolonged cyclic stability and specific energy capacity. Yan, et al reported that Fe_3O_4 NPs with carbon coated can significantly increase the electrical conductivity of Fe_3O_4 NPs with result a high specific capacity of 730 mAh/g after 300 cycles at a high current density of 2 A/g, and a reversible capacity of 433 mAh/g at an ultrahigh rate of 10 A/g [16].

Therefore, research using Fe_3O_4@C material doped with Mn atoms as the battery cathode and Zn as the battery anode to form a Zn-$Mn_{0.25}Fe_{2.75}O_4$@C battery is necessary. Sunaryono et el. has conducted doping optimization that obtained optimum magnetothermal activity at $Mn_{0.25}Fe_{2.75}O_4$ [17], [18]. Core-shell carbon is also an alternative as a conductivity-enhancing alloy in its electrical properties [19]. Then, similar research was conducted regarding the fabrication of Zn-Fe_3O_4@C battery electrodes

with flexible characteristics based on zinc-ion batteries. However, in that study, the specific capacity of Zn-Fe_3O_4@C batteries at a current of 100 mA g^{-1} maintained more than 58 mAh g^{-1} with ~100% Coulombic efficiency over 200 cycles, and the capacity retention after 200 cycles was 81% of the initial capacity of 66 mAh g^{-1}. [20] Therefore, further development of this research is needed with the hope of producing iron sand-based battery electrodes with increased magnetic and electrical properties through Mn doping that is approaching or even higher than batteries on the market. This research focuses on the influence of carbon mass variation in Zn-$Mn_{0.25}Fe_{2.75}O_4$@C battery electrodes fabricated using the spin coating method. Then, the focused analyses include crystal structure analysis, nanocomposite magnetic property analysis, morphology analysis, battery electrode magnetic property analysis, and voltammetry cycle analysis (CV) in Zn-$Mn_{0.25}Fe_{2.75}O_4$@C battery electrodes.

2. Experimental Method

a. Materials

Natural iron sand from Sine Beach, Hydrogen chloride (HCl, 12.063 M, Merck Germany), ammonium hydroxide (NH_4OH, 6.5 M, Merck Germany), $MnCl_2{\cdot}4H_2O$ (197.90 g/mol, Merck Germany), DI Water (WaterOne), Ethylene Glycol (Merck Germany), Nitric Acid (65% Merck Germany), multi-walled carbon nanotubes (MWCNT 3-15 nm), Carbon Black, poly vinylidene fluoride (PVDF 99.5% Arkema), N-methyl-2-pyrrolidone (NMP, Mw 99.13 Merck Germany), Ti-foil (thickness 0.05 mm), Zn-foil (thickness 0.05 mm).

b. Synthesis of $Mn_{0.25}Fe_{2.75}O_4$ Nanoparticles

Natural sand from Sine Beach, Tulungagung, Indonesia is washed with distilled water and dried in the sun until completely dry. The dry sand is then separated using a permanent magnet to obtain a pure iron sand powder. 20 grams of pure iron sand powder are reacted with 58 mL of HCl using a magnetic stirrer hotplate at a temperature of 25 °C and a rotation speed of 720 rpm for 30 minutes. The solution is then filtered to obtain $FeCl_2$ and $FeCl_3$ solutions. The $FeCl_2$ and $FeCl_3$ solutions are mixed with 0.544 grams of $MnCl_2$ powder and stirred for 15 minutes at 720 rpm at room temperature. The solution is titrated with 25 mL of NH4OH on a hotplate for 30 minutes. The resulting mixture is filtered and then washed with distilled water until the pH reaches 7. After filtering, it is calcined at a temperature of 100 °C for 1 hour. The calcination results are then ground using a mortar.

c. Synthesis of $Mn_{0.25}Fe_{2.75}O_4$@C Nanocomposite

The pure $Mn_{0.25}Fe_{2.75}O_4$ nanoparticles obtained were dispersed in 50 mL of DI water to prepare for the next step. 5 mL of $Mn_{0.25}Fe_{2.75}O_4$ nanoparticle seed solution, 1 mL of ethylene glycol, and 20 mg of sucrose were thoroughly mixed with 35 mL of DI water in a 100 mL glass beaker. They were then transferred to a special 50-mL Teflon container, which was sealed in a stainless-steel autoclave. The autoclave was heated to 160 °C in a drying oven for 4 hours to grow the carbon shell. The purified core-shell $Mn_{0.25}Fe_{2.75}O_4$@C nanoparticles were obtained by repeated centrifugal washing in DI water. The obtained $Mn_{0.25}Fe_{2.75}O_4$@C core-shell nanoparticles were treated with nitric acid (5 mol/L) for 1 hour and then repeatedly centrifugally washed in DI water until neutral. The powder sample was prepared by drying in a vacuum furnace. The sample code and composition of carbon is shown in Table 1.

Table 1. The sample code and composition of carbon on $Mn_{0.25}Fe_{2.75}O_4$@C nanoparticles

Carbon compositions	Sample Variation Code
Carbon mass variation 2% in $Mn_{0.25}Fe_{2.75}O_4$@C nanocomposite	MFC1
Carbon mass variation 4% in $Mn_{0.25}Fe_{2.75}O_4$@C nanocomposite	MFC2
Carbon mass variation 6% in $Mn_{0.25}Fe_{2.75}O_4$@C nanocomposite	MFC3
Carbon mass variation 8% in $Mn_{0.25}Fe_{2.75}O_4$@C nanocomposite	MFC4
Carbon mass variation 10% in $Mn_{0.25}Fe_{2.75}O_4$@C nanocomposite	MFC5

d. Fabrication of Zn-$Mn_{0.25}Fe_{2.75}O_4$@C Thin Films

The preparation process for the $Mn_{0.25}Fe_{2.75}O_4$@C electrode is as follows: $Mn_{0.25}Fe_{2.75}O_4$@C powder, MWCNT, carbon black, and PVDF are mixed in a mass ratio of 28:7:10:5 in NMP. The obtained mixture is then coated onto a Ti-foil substrate using a spin coater at 3000 rpm for 30 seconds. After that, the mixture is dried in a vacuum oven at 70 °C for 12 hours, and the substrate is then cooled. The fabrication process for the Zn electrode is similar to that of the $Mn_{0.25}Fe_{2.75}O_4$@C electrode. Zinc powder, MWCNT, and PVDF are mixed in a mass ratio of 8:1:1 in NMP. The obtained mixture is then coated onto a Zn-foil substrate using a spin coater at 300 rpm for 30 seconds. After that, the mixture is dried in a vacuum oven at 70 °C for 12 hours.

e. Characterization

The characterization methods used in this research include X-ray Diffraction (XRD, PANalytical X'Pert PRO Cu-Kα 1.5406 Å) for characterizing the crystal structure, Fourier Transform Infrared Spectroscopy (FTIR, SHIMADZU IRPrestige21) for identifying functional groups, Vibrating Sample Magnetometry (VSM) for analyzing magnetic properties, Transmission Electron Microscopy (TEM TEM JEOL JEM 1400) for observing morphology, Cycling and Durability Testing (CD) for testing battery cycles, and Cyclic Voltammetry (CV) using Potensiostat Correst CS350M for assessing the electrochemical performance of the battery cells. The data analysis methods involve several techniques and software tools. The XRD data is analyzed using *Rietica* to determine the particle size and lattice parameters of the Zn-$Mn_{0.25}Fe_{2.75}O_4$@C nanocomposite. VSM OXFORD 1.2 H recorded from -30 until 30 kOe data is resulted the hysteresis curves to get information about magnetic properties of the samples and analyze using the Langevin Type 2 model. CV curves are used to calculate specific capacitance and energy density. TEM data is analyzed with Image J to evaluate particle size distribution and morphology. The galvanostatic Neware BTS4000 5V6A was used to charge-discharge of samples and conducted to assess battery lifespan, with data analyzed using Origin to determine battery capacity.

1. Result and Discussion

a. Functional Groups of $Mn_{0.25}Fe_{2.75}O_4$@C Nanocomposite

Characterization using the FTIR instrument was conducted to determine the functional groups of both bending and stretching bonds in the samples. In this study, FTIR characterization was performed on each $Mn_{0.25}Fe_{2.75}O_4$ sample and five variations of carbon mass in the $Mn_{0.25}Fe_{2.75}O_4$@C nanocomposites. The FTIR characterization results of the $Mn_{0.25}Fe_{2.75}O_4$ sample are shown in Figure 1. In the functional groups of O-H, C-O, Fe-O, and Mn-O at 3386 cm^{-1}, the O-H stretch is typically associated with hydroxyl groups. These are present due to surface hydroxylation of the material or adsorbed moisture [21], [22], [23], [24]. The C-O bond at 2303 cm^{-1} is due to carbonates or carboxyl groups that have formed during sample preparation or due to the interaction with CO_2 in the atmosphere [25][26]. The Fe-O stretching vibration at 420 cm^{-1} is a characteristic of ferrite structures, confirming the presence of Fe in the oxide lattice [23], [24], [25]. The Mn-O bond at 451 cm^{-1} is indicative of manganese oxide, confirming the Mn content in the ferrite structure [26] [27] [28], confirming the $Mn_{0.25}Fe_{2.75}O_4$ material. Subsequently, the FTIR characterization results of the $Mn_{0.25}Fe_{2.75}O_4$@C nanocomposites are also shown in Figure 1. Hydroxyl groups O-H, Mn-O, Fe-O, C-O, C=C, C-N, and C=O were observed in the five samples at 3572–3672 cm^{-1}.

Similar to the $Mn_{0.25}Fe_{2.75}O_4$ sample, the O-H stretch indicates the presence of hydroxyl groups, likely due to surface hydroxylation or moisture. The Mn-O stretch at 420–441 cm^{-1} confirms the incorporation of manganese within the ferrite structure [23], [24], [25]. The Fe-O stretch at 414–460 cm^{-1} reaffirms the presence of iron oxide within the composite. [23], [29], [30]. The presence of C-O stretching vibrations at 2301-2309 cm^{-1} is likely due to carbonates or carboxyl groups, which are more prominent in the carbon-coated samples [25][26]. The C=C stretch at 1626–1637 cm^{-1} indicates the presence of sp_2 hybridized carbon, typical of graphitic or aromatic structures in the carbon coating [31][32]. The C-N stretch at 1447–1467 cm^{-1} suggests the presence of nitrogen-containing functional groups, which were introduced during synthesis or due to the carbon source used [33], [34], [35]. The C=O stretch at 1663–1683 cm^{-1} indicates carbonyl groups, which are common in oxidized carbon materials and can form due to exposure to air or specific synthesis conditions, respectively, confirming the $Mn_{0.25}Fe_{2.75}O_4$@C nanocomposites.

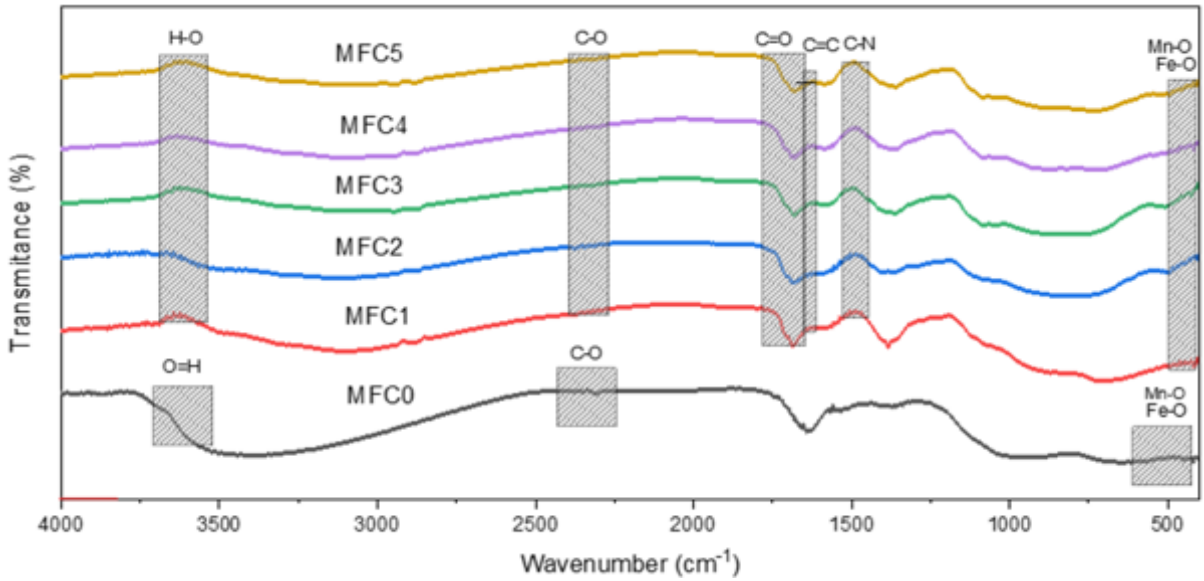

Figure 1. FTIR spectra of $Mn_{0.25}Fe_{2.75}O_4$, and $Mn_{0.25}Fe_{2.75}O_4$@C samples (MCF1, MCF2, MCF3, MCF4, MCF5).

Thus, in the FTIR characterization of two types of samples, $Mn_{0.25}Fe_{2.75}O_4$, and five variations of carbon mass in the $Mn_{0.25}Fe_{2.75}O_4$@C material, the obtained results indicate the presence of specific bonding functional groups in each sample. Comparison between $Mn_{0.25}Fe_{2.75}O_4$ and $Mn_{0.25}Fe_{2.75}O_4$@C: In $Mn_{0.25}Fe_{2.75}O_4$, functional groups O-H, C-O, Fe-O, and Mn-O were detected. In $Mn_{0.25}Fe_{2.75}O_4$@C, in addition to the detected groups in $Mn_{0.25}Fe_{2.75}O_4$, there were additional groups of C-O, C=C, C-N, and C=O, indicating the presence of carbon in the material.

FTIR characterization provides information about bonding functional groups in both types of samples. Table 2 illustrates that the addition of carbon to $Mn_{0.25}Fe_{2.75}O_4$ forms additional bonding groups, such as C-O, C=C, C-N, and C=O. Variations in carbon mass in $Mn_{0.25}Fe_{2.75}O_4$@C result in changes in the intensity and position of bonding functional group peaks, indicating the influence of these variations on the material's chemical structure. This discovery offers further insight into the chemical properties and structure of $Mn_{0.25}Fe_{2.75}O_4$ material and carbon mass variations in $Mn_{0.25}Fe_{2.75}O_4$@C material [36][37][17][19].

Table 2. Functional Groups of $Mn_{0.25}Fe_{2.75}O_4$ and $Mn_{0.25}Fe_{2.75}O_4$@C.

Functional Group	Wavenumber (cm^{-1}) Data					References
	$Mn_{0.25}Fe_{2.75}O_4$					
O-H	3618					3300-3600 [21][22][23][24]
C-O	2303					2300-2310 [25][26]
Fe-O	420					411-460 [38][30][25][29]
Mn-O	451					419-531 [26] [27][28]
	$Mn_{0.25}Fe_{2.75}O_4$@C					
Functional Group	MFC1	MFC2	MFC3	MFC4	MFC5	References
O-H	3572	3638	3618	3588	3598	3000-4000 [21][22][23][24]
Mn-O	433	441	420	427	423	419-531 [26][27][28]
Fe-O	460	414	451	458	444	411-460 [38][30][25][29]
C-O	2309	2305	2309	2309	2301	2300-2310 [25][26]
C=C	1630	1637	1631	1626	1636	1625-1642 [31][32]
C-N	1464	1467	1464	1450	1447	1400-1470 [33][34][35]
C=O	1670	1663	1673	1683	1674	1670 -1687 [39][40][41]

b. Crystal Structure of $Mn_{0.25}Fe_{2.75}O_4$@C Nanocomposite

Characterization using an XRD instrument was used to get information about the phase formed in the diffraction pattern between the *2θ* angle and intensity. Other information that can be obtained includes crystallographic data such as crystal system, space group, lattice parameters *a, b, c, α, β*, and *γ*, as well as the atomic coordinates of each phase found. This can be found after further analysis using the Rietveld method, which utilizes crystallographic databases and performs refinement. Figure 2 is the XRD pattern of $Mn_{0.25}Fe_{2.75}O_4$ and $Mn_{0.25}Fe_{2.75}O_4$@C samples.

In Figure 2, peaks of the Fe_3O_4 phase are identified with small black circles (●) marked. These peaks indicate that $Mn_{0.25}Fe_{2.75}O_4$ is in the crystal phase based on the Fe_3O_4 phase. Carbon is in the amorphous phase materials. The amorphous phase cannot be detected in XRD analysis due to its amorphous nature, which lacks a regular crystalline structure. When X-rays pass through the sample, it resulting diffraction pattern is a result of the crystal patterns generated by the arrangement of atoms in the sample [42]. In this case, carbon peak was not detected because the composition of carbon in sample to low. In sample MFC1, MFC2, MFC3, MFC4, and MFC5, composition carbon is about 2, 4, 6, 8, and 10%, respectively from overall total mass of samples. The $Mn_{0.25}Fe_{2.75}O_4$ phase exhibits a cubic crystal structure with lattice parameters *a=b=c, α=β=γ=90°,* space group Fd3m, and five major peaks on the Bragg planes (220), (311), (400), (511), and (440), as reported in previous studies [43], [44], [45]. After refinement using model data from the American Mineralogist crystal structure database no. 0002400, additional information was obtained: lattice parameters *a = b = c = 8.344–8.385 Å*. As for the crystal size values, they range from 6.10 to 11.53 nm. The detailed information is shown in Table 3.

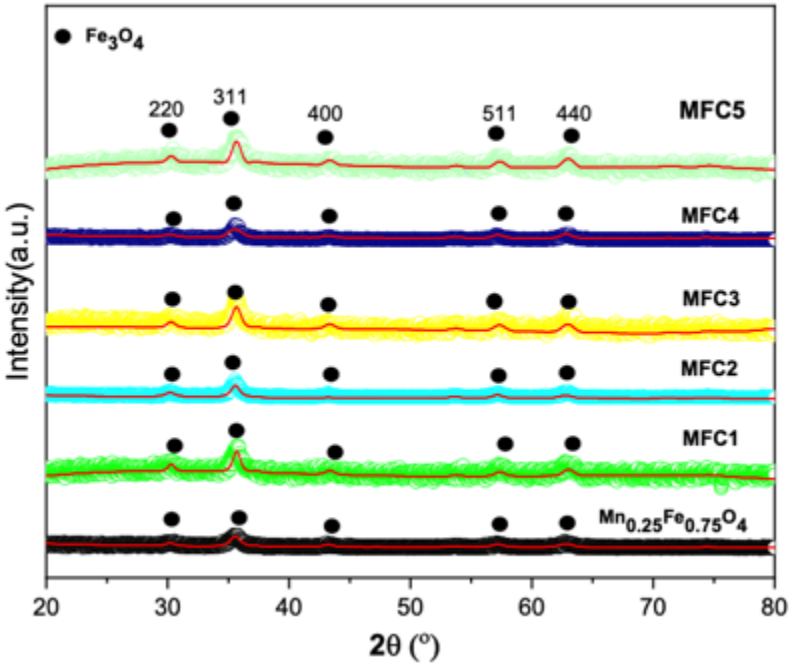

Figure 2. X-ray diffraction patterns of $Mn_{0.25}Fe_{2.75}O_4$ and $Mn_{0.25}Fe_{2.75}O_4$@C nanoparticles.

Table 3. Lattice parameters of $Mn_{0.25}Fe_{2.75}O_4$, and $Mn_{0.25}Fe_{2.75}O_4$@C nanoparticles.

Sample	*Rp*	*Rwp*	χ^2	Lattice parameters *a=b=c* (Å)	Crystal size (nm)
$Mn_{0,25}Fe_{2,75}O_4$	20.85	28.30	1.299	8.369	8.42
MFC1	21.36	29.47	1.292	8.386	10.45
MFC2	21.22	29.44	1.336	8.385	6.10
MFC3	20.44	28.35	1.155	8.364	10.19
MFC4	5.07	6.44	1.039	8.350	8.95
MFC5	4.33	5.42	1.522	8.347	11.53

Table 3 presents the lattice parameters of $Mn_{0.25}Fe_{2.75}O_4$ and $Mn_{0.25}Fe_{2.75}O_4$@C MFC1, MFC2, MFC3, MCF4, and MFC5 samples from XRD analysis. The parameters include *Rp, Rwp, χ2,* lattice parameters *a=b=c (Å),* and crystal size (nm) [46]. The data show that adding carbon affects lattice parameters and crystal sizes. $Mn_{0.25}Fe_{2.75}O_4$ has a lattice parameter of 8.369 Å and a crystal size of 8.42

nm. Carbon addition generally increases crystal size and alters lattice parameters, with MFC4 having the best model fit (χ^2 = 1.039) and MFC5 showing the largest crystal size (11.53 nm). the rise and fall in lattice parameters and crystal sizes are primarily due to the complex interplay between carbon doping, structural distortion, variations in carbon content, potential formation of secondary phases, and experimental conditions. These factors collectively influence the final structure of the nanocomposites, leading to the observed variations [47][48].

c. Morphology of $Mn_{0.25}Fe_{2.75}O_4$@C Nanocomposites

The $Mn_{0.25}Fe_{2.75}O_4$@C nanocomposite was characterized by TEM to determine the particle size and morphology formed in the samples tested. The characterization results obtained are in the form of images up to manometers size. TEM data analysis was carried out using ImageJ software. Then it was plotted using Origin software to determine the particle size distribution of samples MFC3 and MFC5. The results of TEM data analysis for samples MFC3 and MFC5 show an average particle size of 11.5 nm, which is similar to the XRD crystal size of $Mn_{0.25}Fe_{2.75}O_4$@C in this experiment (~ 6 –13 nm) and from other experiments reported previously [49]. Evidence of the aggregation process in magnetite nanoparticles is shown in Figure 3, showing that the nanoparticles tend to cluster due to the strong attraction between one secondary particle and other similar secondary particles.

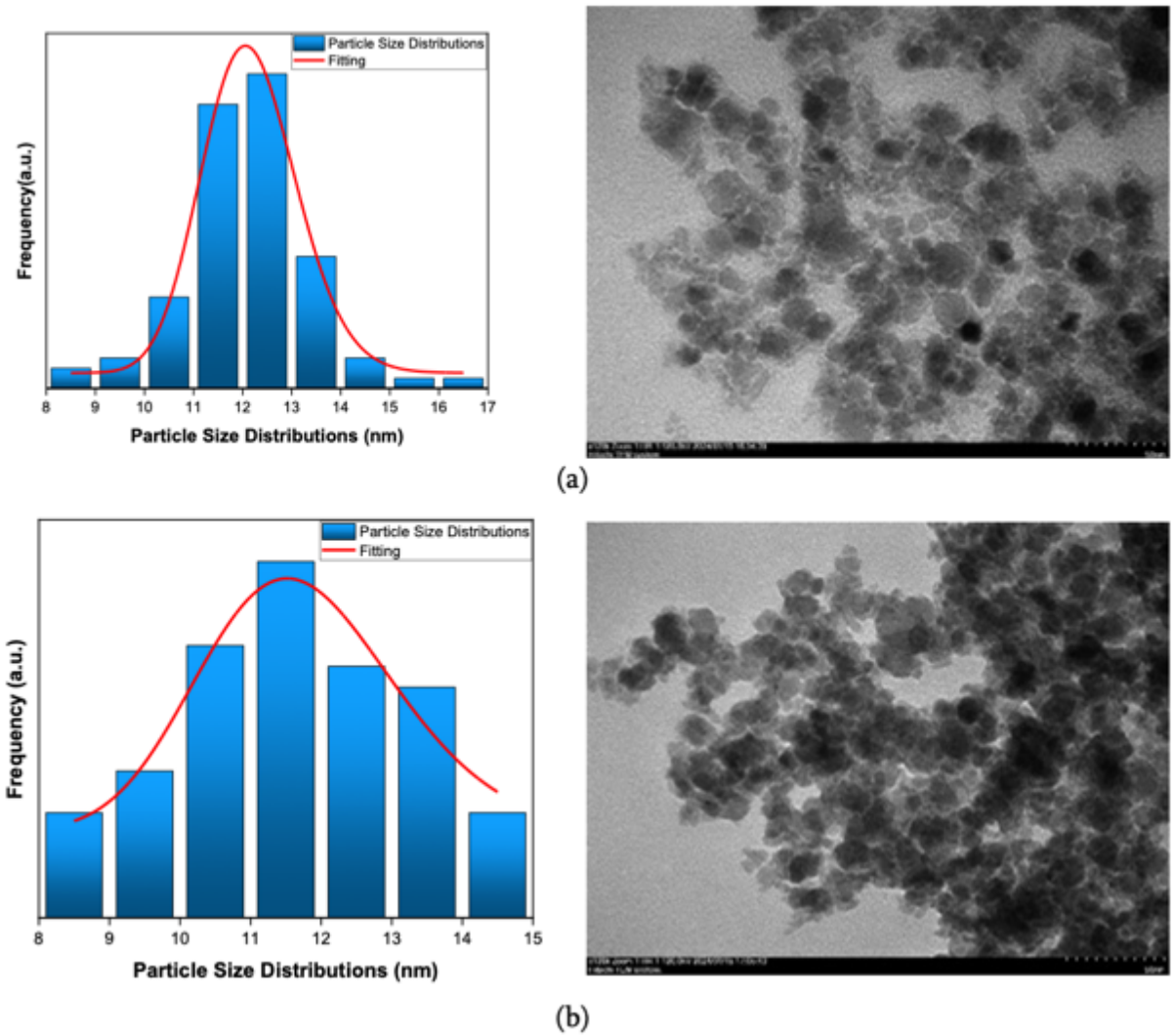

Figure 3. The particle size distribution histograms and TEM images of (a) MFC3 and (b) MFC5 samples.

Composition of carbon in $Mn_{0.25}Fe_{2.75}O_4$@C samples to low (2-10% mass of carbon in the total mass of samples). This is confirmed by the TEM image in Figure 3. Figure 3 shows that the material with a light image is dominant over the darkness. This caused the atomic number of dominant elements in the sample. The dominant element in the sample is Fe (atomic number = 26) because contains

$Mn_{0.25}Fe_{2.75}O_4$ and C for carbon (atomic number = 6). The higher of number of atoms, the higher the lightness image. Otherwise, the lower atomic numbers resulted in a darkness image. So, this confirms that the composition of carbon is lower than $Mn_{0.25}Fe_{2.75}O_4$.

d. Magnetic Properties of $Mn_{0.25}Fe_{2.75}O_4$@C Nanocomposite

VSM is an instrument used to measure the magnetic properties of a sample. When a sample is placed in a magnetic field, VSM can measure the magnetic response of the sample. This magnetic response is expressed in magnetization units, which describe how much magnetization the sample produces in a given magnetic field. The hysteresis curve of test results using VSM for all samples in this study is shown in Figure 4. Further analysis of Figure 4 is carried out using the Langevin equation which corresponds to Equation 1 [50].

$$M = M_s \left[\coth\left(\frac{\mu H}{k_B T}\right) - \frac{k_B T}{\mu H}\right] + \chi H + M_r \quad (1)$$

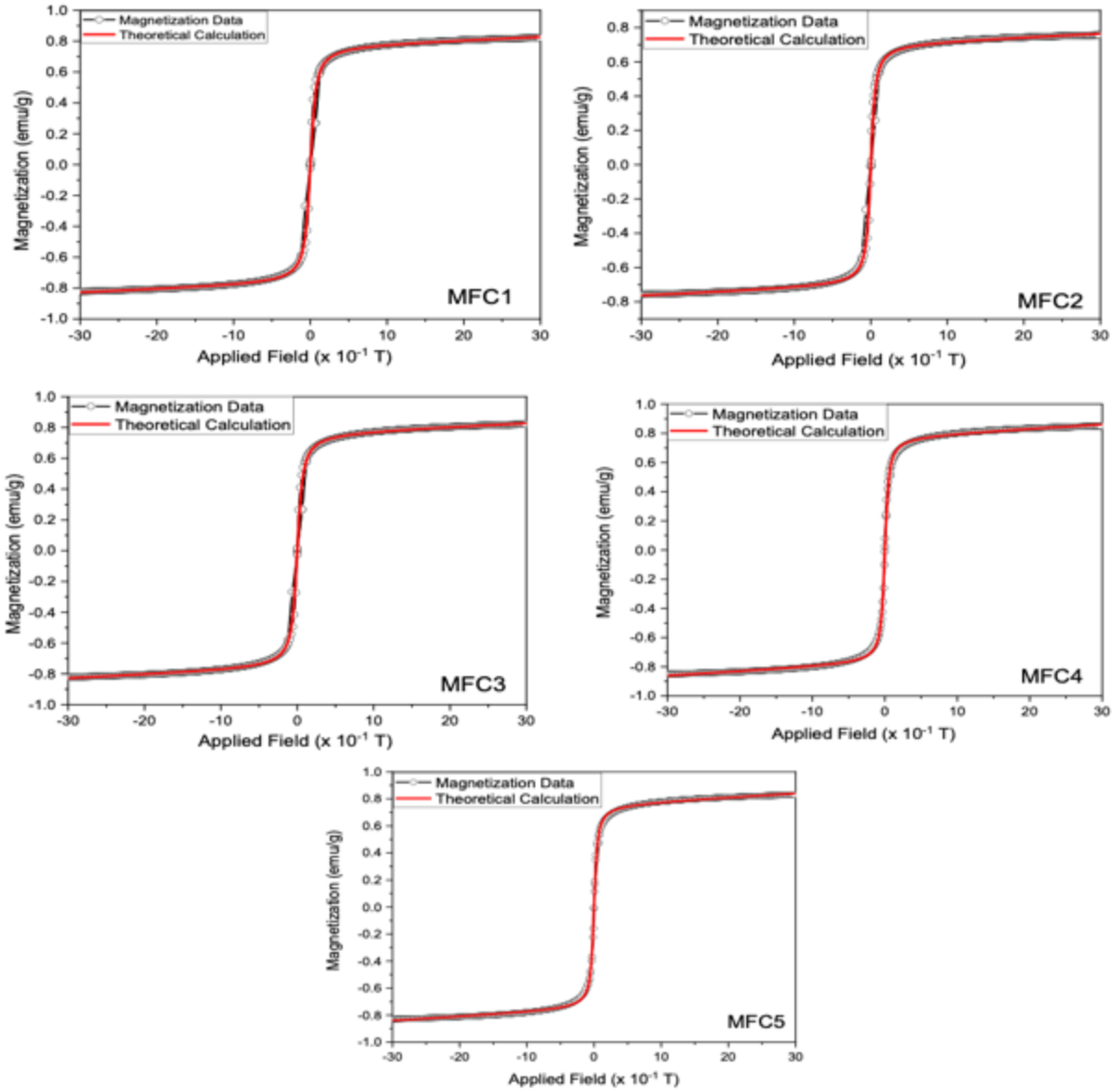

Figure 4. Hysteresis curves and their fitting lines using Langevin equation of the $Mn_{0.25}Fe_{2.75}O_4$@C: MFC1, MFC2, MFC3, MCF4, and MFC5 samples.

where M is the total of magnetizations, M_s is magnetization saturations, M_r is magnetization remanent, χ is susceptibility, and μ is magnetic moment. The results of the analysis in Figure 4 are presented in Table 4. It can be seen that H_c is a measure of the strength of the external magnetic field required to cancel the remanent magnetization of a material. The higher the value of H_c, the more difficult it is to

cancel remanent magnetization, meaning to remove the magnetization remaining in the material after the external magnetic field is removed or turned off, and the stronger the material is as a permanent magnet.

From Figure 4 we can draw several conclusions that there are variations in the coercivity values *(M_s, H_c, and M_r)* between the $Mn_{0.25}Fe_{2.75}O_4$@C nanocomposite samples. This indicates that the magnetic properties of each sample can vary, possibly due to differences in the synthesis process or experimental conditions [51]. Uniform Range of Values: Despite variations, the range of coercivity values for each parameter *(M_s, H_c, and M_r)* is relatively uniform among samples. This shows that despite variations, all samples have consistent magnetic properties within a certain range [52][53]. Inconsistent Behavior Patterns: Note that there are inconsistent changes in coercivity values between samples. For example, M_s and H_c values can increase or decrease from one sample to another. This shows that the factors influencing the magnetic properties may vary between the samples [54]. Importance of Magnetic Analysis: Coercivity data can provide valuable insight into the magnetic properties of $Mn_{0.25}Fe_{2.75}O_4$@C nanocomposite materials. Understanding variations in coercivity between samples can help in optimizing the synthesis process and further understanding the properties of the material [55][52]. Based on the data provided, we can conclude that the type of magnet formed is a superparamagnetic magnet. This can be indicated by the values of H_c and M_r in Table 4 Superparamagnetic is a form of magnetism that appears in small ferromagnetic or ferrimagnetic nanoparticles. In small enough nanoparticles, the magnetization can change direction randomly under the influence of temperature [50]. The influence of carbon on the $Mn_{0.25}Fe_{2.75}O_4$@C nanocomposite material may affect its magnetic properties. Carbon is usually introduced in the form of a layer of carbon that coats or mixes the magnetic material.

Table 4. The magnetic parameters of $Mn_{0.25}Fe_{2.75}O_4$@C nanocomposite samples.

sample	M_s (emu/g)	H_c (T)	M_r (emu/gr)	χ	$\mu \times 10^{-23}$ (J/T)
MFC1	0.88	0.002	0.048	0.00193	2.724
MFC2	0.75	0.002	0.045	0.00196	3.246
MFC3	0.82	0.001	0.041	0.00218	3.302
MFC4	0.85	0.001	0.036	0.00278	4.062
MFC5	0.83	0.001	0.029	0.00284	4.249

Table 4 shows that the M_s value of the sample is in the range of 0.75-0.88 emu/g, with MFC1 having the highest M_s value and MFC2 having the lowest M_s value. The M_s value shows how much magnetization a material can achieve when subjected to a very strong magnetic field. Thus, MFC1 has better magnetization ability compared to MFC2, MFC3, MFC4, and MFC5. Meanwhile, the H_c value of all of the samples is in the range of 0.001-0.002 T, with MFC1 and MFC2 having almost the same H_c value. The H_c value shows how large a magnetic field is needed to demagnetize a material. Thus, MFC1 and MFC2 have lower H_c values compared to MFC3, MFC4, and MFC5. The M_r value for each nanocomposite sample is in the range of 0.029-0.048 emu/g, with MFC1 having the highest M_r value and MFC5 having the lowest M_r value. Retention magnetization indicates how much magnetization a material can maintain when subjected to a weak magnetic field. Thus, MFC1 can resist magnetization better than MFC5. Thus, the influence of carbon on the $Mn_{0.25}Fe_{2.75}O_4$@C nanocomposite material may affect to value of several magnetic parameters. Carbon is usually introduced in the form of a layer of carbon that coats or mixes the magnetic material. So, the addition of more carbon to the $Mn_{0.25}Fe_{2.75}O_4$@C nanocomposite material can cause a decrease in the magnetization, coercivity, and magnetic remanence values because carbon can disrupt the crystal structure and magnetic properties of the original material [24], [50].

e. Cyclic Voltammetry

Measurements using CV aim to determine the reduction-oxidation process in the anode. Measurements were carried out on Zn-$Mn_{0.25}Fe_{2.75}O_4$@C thin films with MFC2, MCF3, and MFC4 samples with the scan rate set at 100 mVs. The voltammogram graph by CV measurement of the samples in this study is shown in Figure 5.

Figure 5 shows that the Zn-$Mn_{0.25}Fe_{2.75}O_4$@C thin films especially MFC2, MFC3, and MFC4 samples provide deep insight into the electrochemical properties and potential for application as battery

electrode materials [56][57]. Oxidation reactions are processes in which atoms or molecules lose electrons, which in turn causes an increase in potential. The anodic peak in the voltammogram is the point where the oxidation level reaches its peak, indicating the occurrence of a significant oxidation reaction in the material [58][59]. The position of the anodic peak in the voltammogram of the Zn-$Mn_{0.25}Fe_{2.75}O_4$@C thin films for sample MFC2 was found to range from 0 to 0.872 V, while for MFC3 it ranged from 0 to 0.757 V, and for MFC4 it ranged from 0 to 0.64 V. Previous research found that the anodic peak position for Fe_3O_4 is between 0 to 0.5 V. The similarity of these positions indicates that the Zn-$Mn_{0.25}Fe_{2.75}O_4$@C thin films especially MFC2, MFC3, and MFC4 samples have similar electrochemical properties to Fe_3O_4, which can provide additional insight into the potential use of this material in battery applications [60][61].

In addition to position, peak current and voltage values on a voltammogram also indicate the electrochemical quality of the material. Peak current reflects the rate of electrochemical reactions occurring on the electrode surface, while peak voltage indicates the energy released or absorbed during the reaction. High peak current and voltage values indicate that the material has a good electrochemical response, which in turn indicates its potential ability to be used in battery applications [62]. A high peak current indicates that the material can support a large current flow, which is a desirable characteristic in high-power battery applications. Meanwhile, a good peak voltage indicates that the material is capable of storing energy efficiently during the charging and discharging process, which is important to ensure stable and reliable battery performance [56][63].

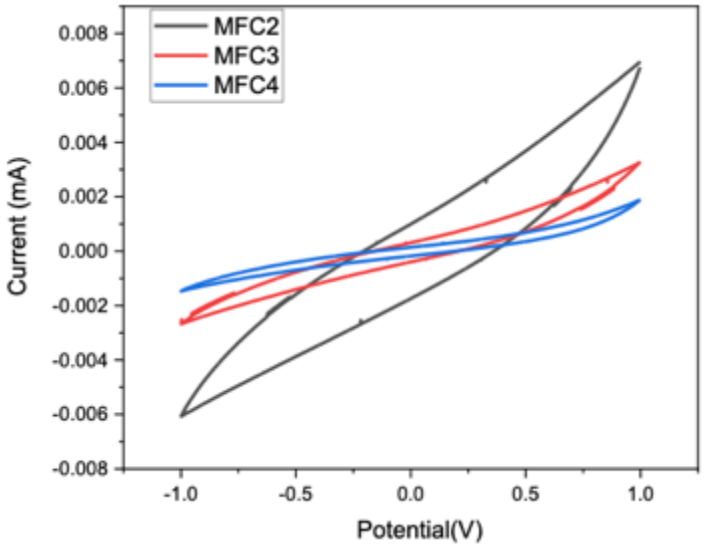

Figure 5. The voltammogram graph of Zn-$Mn_{0.25}Fe_{2.75}O_4$@C MFC2, MFC3, and MFC4.

The presence of an anodic peak in the voltammogram shows that this material has electrochemical properties that support oxidation reactions, which are important in the battery charging and discharging process. The similarity of the anodic peak position with Fe_3O_4 also indicates that this material has electrochemical properties similar to the materials that have been studied [62][56]. In addition, good peak current and voltage values indicate that this material has high electrochemical qualities, which strengthens the argument for its use in battery applications. The ability of materials to support large currents and store energy efficiently is a key factor in creating reliable and high-performance batteries [57]. The measurement results show the presence of an anodic peak which indicates the occurrence of an oxidation reaction, as well as good peak current and voltage values which indicate high electrochemical quality [64].

f. Charge-discharge

The charging-discharging test aims to determine the specific capacitance of the material being tested. Specific capacitance is obtained by dividing the test results in the form of capacitance by the mass of the active material. The test was carried out at a current of 0.1 mV/s and a scan rate of 0.1 C. The test results are shown in Figure 6 and Table 5.

From Figure 6, we can see that MCF2 has higher specific capacitance and energy density than MCF3 and MCF4, but its power density is slightly lower than that of MCF3. this is due to Material Structure: MCF2 has a better material structure or more optimal pore configuration, which allows it to accommodate more electrical charge per unit mass, thus having a higher specific capacitance and energy density, this is a Chemical Composition, the chemical composition of a material can affect its ability to hold an electric charge and store energy. MCF2 has a composition that is more favourable for storing electrical charge. [65] [66][67]. Test results show that intermittent charging is effective in maintaining consistent battery performance during charge and discharge cycles. In addition, the use of certain materials, such as Zn-$Mn_{0.25}Fe_{2.75}O_4$@C MFC2, MFC3, and MFC4, can increase the charging and discharging capacity, which in turn increases the overall battery life [68].

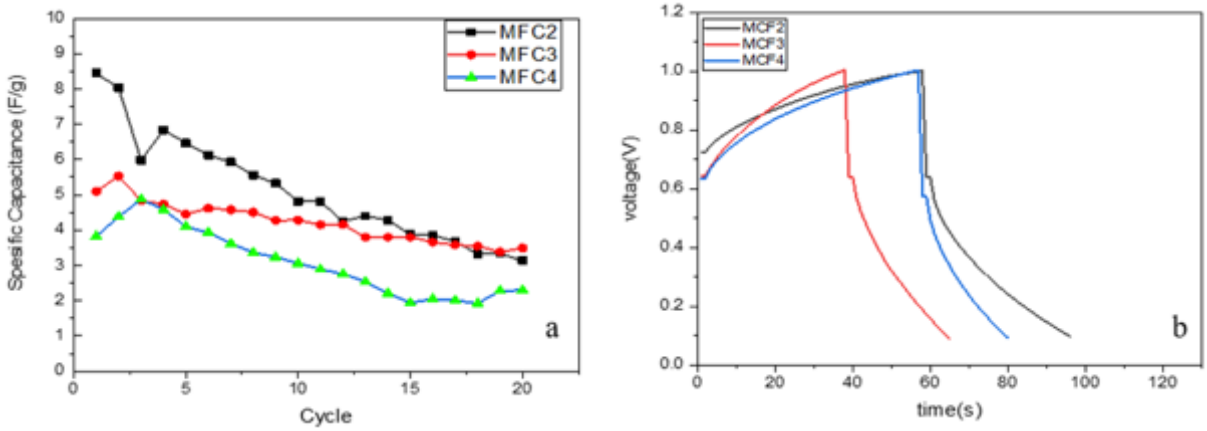

Figure 6. The result of charge and discharge in graph of (a) specific capacitance vs cycles and (b) voltage vs time.

The specific capacitance of supercapacitors is influenced by carbon materials, magnetic properties, and structural characteristics. Carbon materials enhance charge storage and conductivity due to their high surface area and porosity. Magnetic properties improve electrochemical stability and conductivity through synergistic effects. Structural characterization is crucial for understanding performance, with well-ordered crystalline structures facilitating electron transport and unique nanostructures enhancing charge storage. Composite materials combining carbon with metal oxides or conducting polymers exhibit synergistic effects, enhancing capacitance through conductive networks and pseudo-capacitance. Effective integration of these components enables advanced electrode materials with high specific capacitance, rate capability, and stability for supercapacitor applications.[69].

Table 2. Specific capacitance for three samples.

Sample	Specific Capacitance (F/g)	Energy density (Wh/kg)	Power density (W/kg)
MCF2	8.44	1.42	104.40
MCF3	553	0.76	94.35
MCF4	4.87	0.59	88.66

In Table 5 In the results of data analysis of specific capacitance, the test results were analyzed using the Origin application, energy density, and power density of the Zn-$Mn_{0.25}Fe_{2.75}O_4$@C thin films, especially MFC2, MFC3, and MFC4 samples. The MCF2 sample shows the highest maximum specific capacitance (8.44 F/g) and energy density (1.421 Wh/kg), which means a good choice for applications. However, its power density is slightly lower (104.40 W/kg), which may reduce its ability to deliver power quickly. The MCF3, although having lower capacitance and energy density than the MCF2, features a slightly higher power density (94.35 W/kg), making it a good choice for applications where the speed of charging or discharging energy is important. The MCF2 shows good performance in capacitance and energy density but has a slightly lower power density. While MCF3 offers higher power density, but with slight sacrifices in capacitance and energy. The MCF4 displays lower performance overall but can be a more economical or suitable choice for applications with lower performance requirements. Previous research found an energy density of 21.07Wh/kg and a power density of

103.98W/kg[70]. Therefore, the results highlight the importance of considering the specific needs of the intended application when selecting energy storage materials, taking into account the balance between capacitance, energy density, and power density.

The results of data analysis of specific capacitance of MCF2, MCF3, and MCF4 have the opposite result with the value of magnetization saturations and magnetic moment (μ in Table 4). The specific capacitance value decreases when the saturation magnetization and magnetic moment value increases. The large saturation magnetization and magnetic moment value causes the magnetic moment to be unstable. It tends to be more reactive, making it difficult to detect reduction and oxidation reactions during charging and discharging occurs. The low values of specific capacitance and energy density in this study are caused by several factors, including the material used is a magnetic material, where the magnetic material itself has low electrical conductivity, thereby limiting the speed of electron transport. So, the percentage of carbon mass has an impact on specific capacitance values.

2. Conclusion

The XRD analysis revealed that the $Mn_{0.25}Fe_{2.75}O_4$ phase exhibits a spinel cubic crystal structure with lattice parameters $a=b=c$, $\alpha=\beta=\gamma=90°$, and space group Fd3m. After refinement, the lattice parameters were determined to be $a = b = c = 8.344–8.385Å$, with particle sizes ranging from 6.10 nm to 11.53 nm. The addition of carbon induced changes in crystal structure and particle size, supporting the hypothesis of an inverse spinel cubic crystal structure in the $Mn_{0.25}Fe_{2.75}O_4$@C nanocomposite. VSM analysis demonstrated that increasing carbon content in the $Mn_{0.25}Fe_{2.75}O_4$@C nanocomposite led to decreased magnetization, coercivity, and magnetic remanence due to disrupting the original material's crystal structure and magnetic properties. This finding supports the hypothesis that higher carbon mass decreases saturation magnetization, remanent magnetization, and coercivity values, affecting both the nanocomposite and the Zn-$Mn_{0.25}Fe_{2.75}O_4$@C battery electrode. TEM analysis indicated an average particle size of approximately 11.5 nm for samples MFC3 and MFC5, consistent with the XRD crystal size of $Mn_{0.25}Fe_{2.75}O_4$@C (~6–13 nm). Evidence of aggregation in magnetite nanoparticles suggests that varying carbon mass alters the morphology and particle size distribution of Zn-$Mn_{0.25}Fe_{2.75}O_4$@C battery electrode layers. CV measurements showed the formation of an anodic peak in Zn-$Mn_{0.25}Fe_{2.75}O_4$@C variations (MFC2, MFC3, MFC4) during battery operation, with peak positions indicating good electrochemical reaction rates and energy efficiency. These results highlight Zn-$Mn_{0.25}Fe_{2.75}O_4$@C's potential as a reliable and high-performance battery anode. Charging-discharging tests revealed that MCF2 exhibited the highest specific capacitance (8.44 F/g) and energy density (1.421 Wh/kg), making it suitable for applications requiring large energy storage per mass. MCF3 showed lower capacitance and energy density but higher power density (94.35 W/kg), making it ideal for applications with high charging speeds. MCF4 displayed lower overall performance but could be a cost-effective choice for applications with lower performance requirements. These findings underscore the importance of selecting energy storage materials based on application needs, considering the balance between capacitance, energy density, and power density. So, this study confirms that adding carbon to the $Mn_{0.25}Fe_{2.75}O_4$@C nanocomposite affects its crystal structure, magnetic properties, morphology, and electrochemical performance.

Acknowledgment

This work was founded by The Internal Founding for research and community service of the State University of Malang with the PTM scheme under contract number 4.4.661/UN32.14.1/LT/2024 on Behalf of the SN Research Team.

References

[1] M. Nasution, "Mengaplikasikan Sel Volta Dalam Pembuatan Baterai Sebagai Penyimpa Energi," *J. Electr. Technol.*, vol. 6, no. 3, pp. 1–3, 2021.

[2] M. Nasution, "Karakteristik Baterai Sebagai Penyimpan Energi Listrik Secara Spesifik," *JET J. Electr. Technol.*, vol. 6, no. 1, pp. 35–40, 2021.

[3] D. Selvakumaran, A. Pan, S. Liang, and G. Cao, "A review on recent developments and challenges of cathode materials for rechargeable aqueous Zn-ion batteries," *J. Mater. Chem. A*, vol. 7, no. 31, pp. 18209–18236, 2019, doi: 10.1039/c9ta05053a.

[4] J. Huang *et al.*, "A self-charging salt water battery for antitumor therapy," *Sci. Adv.*, vol. 9, no. 13, 2023, doi: 10.1126/sciadv.adf3992.

[5] Y. Liu, Y. Qiao, and Y. Huang, "Flower-Like $K_{0.27}MnO_2$ As Cathode Materials for High-Performance Aqueous Sodium-Ion Batteries for High-Performance Aqueous Sodium-ion Batteries," no. October, pp. 2–3, 2013.

[6] L. Suo *et al.*, "'Water-in-salt' electrolyte enables high-voltage aqueous lithium-ion chemistries," *Science*, vol. 350, no. 6263, pp. 938–943, 2015, doi: 10.1126/science.aab1595.

[7] N. Zhang *et al.*, "Rechargeable aqueous zinc-manganese dioxide batteries with high energy and power densities," *Nat. Commun.*, vol. 8, no. 1, pp. 1–9, 2017, doi: 10.1038/s41467-017-00467-x.

[8] H. Pan *et al.*, "Reversible aqueous zinc/manganese oxide energy storage from conversion reactions," *Nat. Energy*, vol. 1, no. October 2017, 2016, doi: 10.1038/nenergy.2016.39.

[9] L. Suo *et al.*, "'Water-in-salt' electrolyte enables high-voltage aqueous lithium-ion chemistries," *Science*, vol. 350, no. 6263, pp. 938–943, 2015, doi: 10.1126/science.aab1595.

[10] C. D. Wessells, S. V. Peddada, R. A. Huggins, and Y. Cui, "Nickel hexacyanoferrate nanoparticle electrodes for aqueous sodium and potassium ion batteries," *Nano Lett.*, vol. 11, no. 12, pp. 5421–5425, 2011, doi: 10.1021/nl203193q.

[11] P. Canepa *et al.*, "Odyssey of Multivalent Cathode Materials: Open Questions and Future Challenges," *Chem. Rev.*, vol. 117, no. 5, pp. 4287–4341, 2017, doi: 10.1021/acs.chemrev.6b00614.

[12] K. E. K. Sun *et al.*, "Suppression of Dendrite Formation and Corrosion on Zinc Anode of Secondary Aqueous Batteries," *ACS Appl. Mater. Interfaces*, vol. 9, no. 11, pp. 9681–9687, 2017, doi: 10.1021/acsami.6b16560.

[13] P. Zhang *et al.*, " A Convenient Method for Synthesis of Fe_3O_4 /FeS 2 as High-Performance Electrocatalysts for Oxygen Evolution Reaction and Zinc-Air Batteries ," *J. Electrochem. Soc.*, vol. 168, no. 3, p. 030517, 2021, doi: 10.1149/1945-7111/abe9ca.

[14] W. Han, Y. Xiao, J. Yin, Y. Gong, X. Tuo, and J. Cao, "Fe_3O_4@carbon nanofibers synthesized from cellulose acetate and application in lithium-ion battery," *Langmuir*, vol. 36, no. 38, pp. 11237–11244, 2020, doi: 10.1021/acs.langmuir.0c01399.

[15] C. Wang *et al.*, "Hierarchical MOF-derived layered Fe_3O_4 QDs@C imbedded on graphene sheets as a high-performance anode for Lithium-ion storage," *Appl. Surf. Sci.*, vol. 509, no. November, p. 144882, 2020, doi: 10.1016/j.apsusc.2019.144882.

[16] Y. Yan *et al.*, "Carbon-coated $MnFe_2O_4$ nanoparticle hollow microspheres as high-performance anode for lithium-ion batteries," *Electrochimica Acta*, vol. 246, pp. 43–50, Aug. 2017, doi: 10.1016/j.electacta.2017.06.020.

[17] Sunaryono *et al.*, "Various magnetic properties of magnetite nanoparticles synthesized from iron-sands by coprecipitation method at room temperature," *Mater. Sci. Forum*, vol. 827, no. August, pp. 229–234, 2015, doi: 10.4028/www.scientific.net/MSF.827.229.

[18] S. Sunaryono, M. F. Hidayat, N. Mufti, S. Soontaranon, and A. Taufiq, "The effect of Mn doping on nano structure and magnetic properties of $Mn_xFe_{3-x}O_4$-PEG/PVP/PVA based ferrogel," *J. Polym. Res.*, vol. 27, no. 9, 2020, doi: 10.1007/s10965-020-02065-w.

[19] K. Saputra, S. Sunaryono, S. Hidayat, H. Wisodo, and A. Taufiq, "Investigation of nanostructural and magnetic properties of $Mn_{0.25}Fe_{2.75}O_4$/AC nanoparticles," *Mater. Today Proc.*, vol. 44, pp. 3350–3354, 2020, doi: 10.1016/j.matpr.2020.11.646.

[20] Z. Wang, Y. Wang, G. Wang, W. Wu, and J. Zhu, "Earth-abundant magnetite with carbon coatings as reversible cathodes for stretchable zinc-ion batteries," *J. Energy Chem.*, vol. 62, pp. 552–562, 2021, doi: 10.1016/j.jechem.2021.04.012.

[21] S. Tabatabai Yazdi, P. Iranmanesh, S. Saeednia, and M. Mehran, "Structural, optical and magnetic properties of $Mn_xFe_{3-x}O_4$ nanoferrites synthesized by a simple capping agent-free coprecipitation route," *Mater. Sci. Eng. B*, vol. 245, no. May, pp. 55–62, 2019, doi: 10.1016/j.mseb.2019.05.009.

[22] N. C. Horti, M. D. Kamatagi, S. K. Nataraj, M. N. Wari, and S. R. Inamdar, "Structural and optical properties of zirconium oxide (ZrO_2) nanoparticles: Effect of calcination temperature," *Nano Express*, vol. 1, no. 1, pp. 0–9, 2020, doi: 10.1088/2632-959X/ab8684.

[23] H. Tju, A. Taufik, and R. Saleh, "Photocatalytic, sonocatalytic, and photosonocatalytic of Fe3O4/CuO/ZnO nanocomposites with addition of 2 different types of carbon," *AIP Conf. Proc.*, vol. 1788, 2017, doi: 10.1063/1.4968384.

[24] W. Yang, J. Xu, L. Niu, J. Zhao, C. Wang, and X. Liu, "Dispersion stability of nano-Sb2O3 particles modified with polyethylene glycol," *Part. Sci. Technol.*, vol. 36, no. 7, pp. 844–849, 2018, doi: 10.1080/02726351.2017.1305027.

[25] Y. A. Muhammad, S. Sunaryono, A. J. W. T. Nenohai, N. Mufti, R. Situmorang, and A. Taufiq, "Adsorption properties of magnetic sorbent $Mn_{0.25}Fe_{2.75}O_4$@SiO_2 for mercury removal," *Key Eng. Mater.*, vol. 851 KEM, pp. 197–204, 2020, doi: 10.4028/www.scientific.net/KEM.851.197.

[26] Sunaryono, N. Miftachul Chusna, A. Taufiq, N. Mufti, and S. Hidayat, "The Influence of Alternating Magnetic Field Frequency on Magneto-Thermal Behavior of Mn0.25Fe2.75O4@PANI Material," *IOP Conf. Ser. Mater. Sci. Eng.*, vol. 515, no. 1, pp. 0–9, 2019, doi: 10.1088/1757-899X/515/1/012035.

[27] J. Amighian, E. Karimzadeh, and M. Mozaffari, "The effect of Mn^{2+} substitution on magnetic properties of $Mn_xFe_{3-x}O_4$ nanoparticles prepared by coprecipitation method," *J. Magn. Magn. Mater.*, vol. 332, pp. 157–162, Apr. 2013, doi: 10.1016/J.JMMM.2012.12.005.

[28] "Department Fourier-transform infrared spectroscopy (FTIR) analysis of triclinic and hexagonal birnessites Florence T. Ling," pp. 1–50, 2017.

[29] Sunaryono, N. Miftachul Chusna, A. Taufiq, N. Mufti, and S. Hidayat, "The Influence of Alternating Magnetic Field Frequency on Magneto-Thermal Behavior of $Mn_{0.25}Fe_{2.75}O_4$@PANI Material," *IOP Conf. Ser. Mater. Sci. Eng.*, vol. 515, no. 1, pp. 0–9, 2019, doi: 10.1088/1757-899X/515/1/012035.

[30] M. Anbarasu, M. Anandan, E. Chinnasamy, V. Gopinath, and K. Balamurugan, "Synthesis and characterization of polyethylene glycol (PEG) coated Fe_3O_4 nanoparticles by chemical co-precipitation method for biomedical applications," *Spectrochim. Acta - Part Mol. Biomol. Spectrosc.*, vol. 135, pp. 536–539, 2015, doi: 10.1016/j.saa.2014.07.059.

[31] H. Li *et al.*, "Hierarchical sandwiched Fe_3O_4@C/Graphene composite as anode material for lithium-ion batteries," *J. Electroanal. Chem.*, vol. 847, no. January, p. 113240, 2019, doi: 10.1016/j.jelechem.2019.113240.

[32] X. Wang *et al.*, "Yolk-double shell Fe_3O_4@C@C composite as high-performance anode materials for lithium-ion batteries," *J. Alloys Compd.*, vol. 822, p. 153656, 2020, doi: 10.1016/j.jallcom.2020.153656.

[33] I. A. Safo, C. Dosche, and M. Oezaslan, "TEM, FTIR and electrochemistry study: Desorption of PVP from Pt nanocubes," *Z. Phys. Chem.*, vol. 232, no. 9–11, pp. 1319–1333, 2018, doi: 10.1515/zpch-2018-1147.

[34] R. Novita and N. P. Putri, "Sintesis Lapisan Tipis PANi/PVA sebagai Bahan Elektrokromik," *Sains Dan Mat.*, vol. 5, no. 2, pp. 29–34, 2017.

[35] A. Gholizadeh, "A comparative study of physical properties in Fe_3O_4 nanoparticles prepared by coprecipitation and citrate methods," *J. Am. Ceram. Soc.*, vol. 100, no. 8, pp. 3577–3588, 2017, doi: 10.1111/jace.14896.

[36] N. Miftachul Chusna, Sunaryono, S. Hidayat, N. Hidayat, N. Mufti, and A. Taufiq, "Identification of Nanostructural and Specific Absorption Rate (SAR) on $Mn_{0.25}Fe_{2.75}O_4$/Ag Nanoparticle Composites," *IOP Conf. Ser. Earth Environ. Sci.*, vol. 276, no. 1, pp. 0–10, 2019, doi: 10.1088/1755-1315/276/1/012062.

[37] N. M. Chusna, J. Wei, Y. Gu, and X. Wu, "Nanoparticles and Their Potential as Hyperthermia Therapy Magneto-Thermal Effect in $Mn_{0.25}Fe_{2.75}O_4$-PEG Nanoparticles and Their Potential as Hyperthermia Therapy," pp. 0–11, 2019, doi: 10.1088/1757-899X/515/1/012008.

[38] A. S. Prasad, "Iron oxide nanoparticles synthesized by controlled bio-precipitation using leaf extract of Garlic Vine (Mansoa alliacea)," *Mater. Sci. Semicond. Process.*, vol. 53, pp. 79–83, 2016, doi: 10.1016/j.mssp.2016.06.009.

[39] S. B. Ghaffari, M. H. Sarrafzadeh, Z. Fakhroueian, S. Shahriari, and M. R. Khorramizadeh, "Functionalization of ZnO nanoparticles by 3-mercaptopropionic acid for aqueous curcumin delivery: Synthesis, characterization, and anticancer assessment," *Mater. Sci. Eng. C*, vol. 79, pp. 465–472, 2017, doi: 10.1016/j.msec.2017.05.065.

[40] S. Venkateswarlu, S. Himagirish Kumar, and N. V. V. Jyothi, "Rapid removal of Ni(II) from aqueous solution using 3-Mercaptopropionic acid functionalized bio magnetite nanoparticles," *Water Resour. Ind.*, vol. 12, pp. 1–7, 2015, doi: 10.1016/j.wri.2015.09.001.

[41] O. P. Gomes *et al.*, "3-Mercaptopropionic acid functionalization of titanium dioxide thin films," *Mater. Chem. Phys.*, vol. 223, no. May 2018, pp. 32–38, 2019, doi: 10.1016/j.matchemphys.2018.10.041.

[42] R. M. H. C. N. Achilles, G. W. Downs, R. T. Downs1, R. V. Morris, E. B. Rampe, D. W. Ming, S. J. Chipera, D. F. Blake, D. T. Vaniman, T. F. Bristow, A. S. Yen, S. M. Morrison, A. H. Treiman, P. I. Craig and and N. C. V. M. Tu, "Modeling analog amorphous phases.," *49th Lunar Planet. Sci. Conf. 2018*, vol. LPI Contri, no. 2083, p. 2661, 2018.

[43] U. Schwertmann and R. M. Cornell, *Iron oxides in the laboratory: preparation and characterization*. John Wiley & Sons, 2008.

[44] A. Choerulla, *et al.*, "Study of the Structure of $Mn_xFe_{3-x}O_4$-Poly(m-Aminobenzene Sulfonic Acid) Composites Based on Natural Sand," *JPSE J. Phys. Sci. Eng.*, vol. 7, no. 1, pp. 16–22, Apr. 2022, doi: 10.17977/um024v7i12022p016.

[45] V. M. Alfianti, *et al.*, "Fabrication and Characterization of GO-Fe_3O_4/PSF Membrane with Phase Inversion Method," *JPSE J. Phys. Sci. Eng.*, vol. 6, no. 2, pp. 55–60, Jul. 2021, doi: 10.17977/um024v6i22021p055.

[46] Sunaryono *et al.*, "Magneto-Thermal Effect in $Mn_{0.25}Fe_{2.75}O_4$-PEG Nanoparticles and Their Potential as Hyperthermia Therapy," *IOP Conf. Ser. Mater. Sci. Eng.*, vol. 515, no. 1, pp. 0–11, 2019, doi: 10.1088/1757-899X/515/1/012008.

[47] Y. Dianti, "済無," *Angew. Chem. Int. Ed. 611 951–952*, pp. 5–24, 2017.

[48] B. C. Hancock and G. Zografi, "Characteristics and Significance of the Amorphous State in Pharmaceutical Systems," *J. Pharm. Sci.*, vol. 86, no. 1, p. 1, 1997, doi: 10.1021/js9601896.

[49] T. Szabó, L. Nánai, D. Nesztor, B. Barna, O. Malina, and E. Tombácz, "A Simple and Scalable Method for the Preparation of Magnetite/Graphene Oxide Nanocomposites under Mild Conditions," *Adv. Mater. Sci. Eng.*, vol. 2018, 2018, doi: 10.1155/2018/1390651.

[50] S. Tabatabai Yazdi, P. Iranmanesh, S. Saeednia, and M. Mehran, "Structural, optical and magnetic properties of MnxFe3–xO4 nanoferrites synthesized by a simple capping agent-free coprecipitation route," *Mater. Sci. Eng. B Solid-State Mater. Adv. Technol.*, vol. 245, no. May, pp. 55–62, 2019, doi: 10.1016/j.mseb.2019.05.009.

[51] T. R. Simbolon *et al.*, "Preparation and characterization of $ZnFe_2O_4$ on the microstructures and magnetic properties," *J. Aceh Phys. Soc.*, vol. 10, no. 2, pp. 32–35, 2021, doi: 10.24815/jacps.v10i2.18710.

[52] A. Musa Rampengan and S. Milian Tompunu Tengker, "Analisa sifat kemagnetan polimer poliethylen glycol (PEG-4000)-coated nanopartikel magnetite Fe_3O_4 menggunakan vibrating sample magnetometer (VSM)," *Fuller. Journ Chem*, vol. 6, no. 2, pp. 161–164, 2021, doi: 10.37033/fjc.v6i2.376.

[53] A. Nikmah, A. Taufiq, and A. Hidayat, "Synthesis and Characterization of HPMC/HAP/Fe_3O_4/SiO_2 Composites for Application," *Sains Materi Indones.*, vol. 21, no. 4, pp. 170–176, 2019.

[54] E. Prayitno, T. Suprawoto, and B. F. Riyanto, "Optimasi Hasil Pencarian Pada Web Scrapping MenggunakanPembobotan Kata Tf-Idf," *J. Innov. Res. Knowl.*, vol. 1, no. 7, pp. 241–246, 2021.

[55] P. Puspitasari, A. A. Permanasari, M. S. Shaharun, and A. Muhammad, "High saturation superparamagnetic properties of low-temperature sintering of nickel oxide," *AIP Conf. Proc.*, vol. 2228, 2020, doi: 10.1063/5.0000884.

[56] O. Gharbi, M. T. T. Tran, B. Tribollet, M. Turmine, and V. Vivier, "Revisiting cyclic voltammetry and electrochemical impedance spectroscopy analysis for capacitance measurements," *Electrochimica Acta*, vol. 343, p. 136109, 2020, doi: 10.1016/j.electacta.2020.136109.

[57] X. Huang *et al.*, "Cyclic Voltammetry in Lithium–Sulfur Batteries—Challenges and Opportunities," *Energy Technol.*, vol. 7, no. 8, 2019, doi: 10.1002/ente.201801001.

[58] D. M. Morales and M. Risch, "Seven steps to reliable cyclic voltammetry measurements for the determination of double layer capacitance," *JPhys Energy*, vol. 3, no. 3, pp. 0–18, 2021, doi: 10.1088/2515-7655/abee33.

[59] S. Aderyani, P. Flouda, S.A. Shah, M.J. Green, J.L. Lutkenhaus, and H. Ardebili. Simulation of cyclic voltammetry in structural supercapacitors with pseudocapacitance behavior. *Electrochimica Acta*. 2021 Sep 10;390:138822, doi:10.1016/j.electacta.2021.138822.

[60] W. Yodying, T. Sarakonsri, N. Ratsameetammajak, K. Khunpakdee, M. Haruta, and T. Autthawong. Low-cost production of Fe_3O_4/C nanocomposite anodes derived from banana stem waste recycling for sustainable lithium-ion batteries. *Crystals*. vol. 13, no. 2, 2023, doi: 10.3390/cryst13020280.

[61] S. Aderyani, P. Flouda, S. A. Shah, M. J. Green, J. L. Lutkenhaus, and H. Ardebili, "Simulation of cyclic voltammetry in structural supercapacitors with pseudocapacitance behavior," *Electrochimica Acta*, vol. 390, p. 138822, 2021, doi: 10.1016/j.electacta.2021.138822.

[62] E. M. Espinoza, J. A. Clark, J. Soliman, J. B. Derr, M. Morales, and V. I. Vullev, "Practical Aspects of Cyclic Voltammetry: How to Estimate Reduction Potentials When Irreversibility Prevails," *J. Electrochem. Soc.*, vol. 166, no. 5, pp. H3175–H3187, 2019, doi: 10.1149/2.0241905jes.

[63] S. Schindler and T. Bechtold, "Mechanistic insights into the electrochemical oxidation of dopamine by cyclic voltammetry," *J. Electroanal. Chem.*, vol. 836, no. January, pp. 94–101, 2019, doi: 10.1016/j.jelechem.2019.01.069.

[64] Richards et al., "Fundamentals of Fast-Scan Cyclic Voltammetry for Dopamine," *Physiol. Behav.*, vol. 176, no. 5, pp. 139–148, 2018, doi: 10.1039/c9an01586h.Fundamentals.

[65] G. Zhong *et al.*, "Nano Energy Epitaxial array of Fe_3O_4 nanodots for high rate high capacity conversion type lithium ion batteries electrode with long cycling life," vol. 74, no. March, pp. 1–9, 2020, doi: 10.1016/j.nanoen.2020.104876.

[66] Ç. Özada, M. Ünal, H. Özer, and M. Yazici, "Development of Mno2/Pani/Swcnt Nanocomposite Supercapacitor Electrode and Investigation of Electrochemical Performance," *Uludağ Univ. J. Fac. Eng.*, vol. 28, no. 3, pp. 887–904, 2023, doi: 10.17482/uumfd.1290797.

[67] Z. Li *et al.*, "Novel Charging-Optimized Cathode for a Fast and High-Capacity Zinc-Ion Battery," *ACS Appl. Mater. Interfaces*, vol. 12, no. 9, pp. 10420–10427, 2020, doi: 10.1021/acsami.9b21579.

[68] K. Hanif, M. Anwar, F. Adriyanto, M. Nizam, and J. S. Saputro, "The Effect of Adding Nanoparticles from the Synthesis of Arc Discharge on the Performance of Lithium Ion Batteries," *E3S Web Conf.*, vol. 465, pp. 3–7, 2023, doi: 10.1051/e3sconf/202346502049.

[69] N. I. H. Razman, S. Endud, and I. I. Misnon, "The effect of oxygen and nitrogen functional groups on the electrochemical performance of ordered carbon," *J. Teknol.*, vol. 81, no. 3, pp. 67–72, 2019, doi: 10.11113/jt.v81.12827.

[70] M. Diantoro *et al.*, "Hierarchical Activated Carbon–MnO_2 Composite for Wide Potential Window Asymmetric Supercapacitor Devices in Organic Electrolyte," *Micromachines*, vol. 13, no. 11, 2022, doi: 10.3390/mi13111989.